



Contents lists available at ScienceDirect

Next Sustainability

journal homepage: www.sciencedirect.com/journal/next-sustainability

Research article

Upcycling can seals into high-value boehmite-like for the synthesis of MnAl_2O_4 : A circular economy approach

Dienifer F.L. Horsth^{a,b,*}, Julia de O. Primo^b, Jamille S. Correa^b, Fauze J. Anaissi^b, Xavier Noirfalise^c, Carla Bittencourt^a^a *Chimie des Interactions Plasma-Surface (ChIPS), Research Institute for Materials Science and Engineering, University of Mons, 7000 Mons, Belgium*^b *Chemistry Department, Universidade Estadual do Centro-Oeste, Guarapuava 85040-167, Brazil*^c *Materia Nova, Av. Nicolas Copernic 3, 7000 Mons, Belgium*

ARTICLE INFO

Keywords:

Recycling
Aluminum
Pigments
Sustainability
Color stability

ABSTRACT

Boehmite is a mineral of aluminum oxyhydroxide widely used as a catalyst support, adsorbent for dyes, and a key component in producing advanced optical and electronic devices. This study focuses on the synthesis of boehmite using recycled metallic aluminum through acid digestion (HCl) and subsequent precipitation by pH correction (NaOH). The aluminum source used was can seals, which were characterized using various techniques, including X-ray diffraction (XRD), scanning electron microscopy (SEM), energy dispersive X-ray spectroscopy (EDS), and X-ray photoelectron spectroscopy (XPS). XRD analysis confirmed a boehmite-like phase of the recycled aluminum oxyhydroxide powder. SEM analysis revealed that the synthesized boehmite-like powder consisted of agglomerate plates, which influences its thermal and optical behavior, resulting in a lower dihydroxylation temperature and smaller band gap (~3.7 eV) compared to the literature value (~5.5 eV) for boehmite. The boehmite-like powder derived from recycling was used as a precursor for the synthesis of manganese aluminate (MnAl_2O_4). XRD analysis confirmed the formation of the MnAl_2O_4 galaxite phase, with XPS and absorbance spectroscopy in the visible region indicating the presence of mainly Mn^{2+} ions. The resulting brown manganese aluminate powder exhibited stability in harsh chemical environments, with a color change imperceptible to the human eye. Moreover, a near-infrared (NIR) reflectance of approximately 50% was achieved, superior to other brown pigments reported in the literature. These findings suggest that recycled aluminum can seals in aluminate have potential applications as pigments for coatings.

1. Introduction

Boehmite (aluminum oxyhydroxide ($\gamma\text{-AlO}(\text{OH})$)) is used as a precursor to obtain different alumina phases (Υ , θ , χ , κ , and $\gamma\text{-Al}_2\text{O}_3$) [1]. Furthermore, it is used in the preparation of optical and electronic devices, as support for catalysts, in cosmetics pigments, and as a dye adsorbent due to the high density of hydroxyl groups on its surface, allowing its modification [1–5]. Boehmite has a layered orthorhombic structure; each layer has compacted cubic oxygen packing. However, the overall structure is not compacted; hydroxyl groups are arranged on the surfaces of the layers, and the layers are held together by hydrogen bonds, with O-H-O distance of approximately 2.70 Å, facilitating surface and interlayer modification [6]. Boehmite can be synthesized by hydrothermal synthesis [7–9], sol-gel process [10,11], hydrolysis of

aluminum solutions in an alkaline medium [12], thermal decomposition [13], microwave [14], electrodeposition [15] and microemulsion [16]. Among these methods, hydrothermal synthesis and sol-gel are the most used. The energy expenditure in hydrothermal synthesis can be large due to the need to maintain high temperatures and pressures during the synthesis. However, the synthesis parameters can be finely controlled to produce a material with high crystallinity [1]. Sol-gel processes, typically initiated from aluminum alkoxides, can yield xerogels or aerogels as end products. Despite the preparation of very pure and reproducible boehmite, the process is costly [10]. Alternatively, metallic aluminum or aluminum salts can be used as a precursor to obtain boehmite via precipitation [17].

Aluminum is the third most abundant element on earth and the second most used metal after iron, although it is not found in its

* Corresponding author at: Chimie des Interactions Plasma-Surface (ChIPS), Research Institute for Materials Science and Engineering, University of Mons, 7000 Mons, Belgium.

E-mail address: dhorst@unicentro.edu.br (D.F.L. Horsth).

<https://doi.org/10.1016/j.nxsust.2023.100009>

Received 15 July 2023; Received in revised form 17 October 2023; Accepted 19 October 2023

Available online 25 October 2023

2949-8236/© 2023 The Authors. Published by Elsevier Ltd. This is an open access article under the CC BY-NC-ND license (<http://creativecommons.org/licenses/by-nc-nd/4.0/>).

elemental form in nature [18]. The high aluminum useableness is associated with its versatile properties; it is a light, conductive, malleable, corrosion-resistant, low density ($\sim 2.70 \text{ g}\cdot\text{cm}^{-3}$), and low melting temperature ($\sim 660 \text{ }^\circ\text{C}$) metal [19]. These characteristics have widely explored this metal in various industry sectors [19]. Currently, the production of aluminum is conducted through two distinct processes: primary aluminum production, which involves the extraction of bauxite, and secondary aluminum production, which involves the utilization of scrap and pre-existing aluminum products [19,20]. For every kilogram of recycled aluminum, approximately 5.4 kg of bauxite is saved, while also preventing the generation of salt dross [21]. Aluminum production has the most significant energy difference between primary production (174–186 MJ/kg) and secondary production (10–20 MJ/kg) [18,20]. The disparity arises due to the utilization of distinct raw materials in the recycling (secondary production) and primary aluminum production processes. In recycling, aluminum scrap serves as the primary material, while in primary aluminum production, bauxite acts as the source material, necessitating energy-intensive extraction methods [19]. The main aluminum recycling process is through smelting, a process wherein a metal is extracted, either as the element or as a simple compound, from its ore through heating beyond the melting point. This process typically occurs in the presence of oxidizing agents, such as air, or reducing agents, such as coke [22]. Moreover, the molten aluminum in the furnace is shielded by a flow of molten salt to protect the metal from the reactive atmosphere and facilitate the agglomeration and separation of the aluminum. The liquid stream completely absorbs the non-metallic components of the raw mixture, and before capturing the molten metal, the top layer (salt dross) is skimmed off. Consequently, over a million tons of salt dross are generated yearly, with approximately 95% of this waste directed to landfills [19,23]. However, it is worth noting that aluminum can also be recycled through chemical treatments, such as acid digestion, exploiting the solubility of aluminum and generating less waste compared to primary aluminum production [24]. According to Abbralatas (2022) [21] and European Aluminum (2022) [25], the annual production of can seals in Brazil is approximately 33.4 billion, with a recycling rate of 98.7%. In contrast, in Europe, the recycling rate drops to 76%. To produce 1 kg of boehmite, approximately 1500 can seals are needed. The future lies in recycling waste to synthesize materials, especially those that come from non-renewable sources. Therefore, aluminum recycling plays a crucial role in conserving natural resources, reducing pollution, saving energy, creating jobs, and promoting a circular economy. This practice can be readily adopted through the correct separation of waste at the household level, active participation in selective waste collection programs, and the provision of incentives for recycling by industry and governments.

Aluminum recycling starts with the selection of the precursor. Here, aluminum can seals were chosen as the precursor. To fully comprehend the recycling process, we conducted a detailed analysis of typical can seals using X-ray photoelectron spectroscopy (XPS), X-ray diffraction (XRD), scanning electron microscopy (SEM), and energy dispersive X-ray analysis (EDX). These analytical methods were used to gather information regarding the composition, morphology, structure, and surface characteristics of the can seals. Subsequently, the obtained boehmite-like material derived from the recycled can seals was examined using thermogravimetric analysis (TGA), ultraviolet–vis spectroscopy (UV–Vis), Photoluminescence, XRD, and SEM. The boehmite-like was then used as a precursor for the synthesis of manganese aluminate, which was studied using XRD, XPS, SEM, UV–Vis, Near-infrared spectroscopy (NIRS), and Colorimetry.

We recently reported using boehmite-like to synthesize aluminate paint pigments [3,26]. The aluminate host can be doped with elements such as Cr, Mn, Fe, Co, and Ni, which results in distinct quadrants on the colorimetric diagram for the a^* and b^* regions. [27]. One notable pigment among the aluminates, particularly in the brown range, is the manganese aluminate (MnAl_2O_4) phase galaxite, exhibiting versatility and a wide range of applications in various industrial sectors. It is widely

recognized as a valuable pigment for ceramics, glass, paints, and coatings, imparting vibrant, long-lasting colors [28]. The brown color of manganese aluminate can provide distinctive shades when incorporated into ceramics and glasses [29]. Furthermore, its role as a catalyst in chemical reactions and its contribution to the manufacture of advanced ceramic materials, permanent magnets, and ferroelectric electronic components highlight its importance in chemistry, electronics, and materials engineering [30]. Its resistance to high temperatures and corrosion also makes it a preferred choice in manufacturing refractory materials for industrial applications [31]. Here, manganese aluminate is produced using recycled aluminum in the form of boehmite-like. The obtained synthetic inorganic pigment was evaluated for its suitability as a pigment for architectural painting, with its color stability in harsh environments and NIR reflectance being assessed.

2. Materials and methods

2.1. Characterization techniques

The samples were characterized by X-ray diffraction (XRD), carried out in an Empyrean from Panalytical, model D2 Phaser, equipped with a copper cathode ($\lambda = 1.5418 \text{ \AA}$), operated at 30 kV, current of 10 mA, with a working window between 10° and 80° (2θ) scanned with step of $0.02 \theta / \text{s}$. A scanning electron microscope Hitachi SU8020 SEM (Tokyo, Japan) equipped with an EDX model 4505A–6UUS–SN, with a resolution of 134 eV (Thermo Scientific), was used to observe the sample morphology and elemental composition. The chemical composition of the samples was evaluated by X-ray photoelectron spectroscopy (XPS) (Versaprobe PHI 5000, Physical Electronics, Chanhassen, MN, USA), equipped with a monochromatic Al $K\alpha$ X-ray source. The EDX typical depth of analysis is about 2 micrometers, while XPS measures the surface layer composition of the material [32]. To conduct XPS depth profile analysis, argon ions with a kinetic energy of 500 V were rastered over $2 \times 2 \text{ mm}^2$ surface area; the ion gun was positioned at an angle of 45° to the surface. For a comprehensive analysis, a thin plate or lamella was prepared by cutting the seal with nippers and polishing the cross-section side with a SiC polishing mat until a smooth, shiny surface was obtained (Fig. 1). The resulting lamella was then washed with isopropanol, and two distinct regions were identified: the top region and the cross-section; both regions were analyzed by XPS and SEM.

Thermogravimetric analysis was performed on a Perkin Elmer® STA 6000 thermal analyzer (Massachusetts, USA), scanning from 30° to 1000°C in an oxygen atmosphere with a 50 mL/min flow rate and a heating rate of $10^\circ\text{C}/\text{min}$. The visible spectra were obtained using the Ocean Optics spectrophotometer (USB 2000), equipped with optical fiber, tungsten-halogen source, and silicon (350–720 nm) and germanium (720–1050 nm) detectors. The band gap was calculated by the Kubelka-Munk method [32] with reflectance measured on the equipment Agilent Cary 5000 UV–vis–NIR spectrometer (Santa Clara, USA). For photoluminescence, a Fluorog-QM-75–22-C from Horiba (Canada) was used. The samples were supported on carbon tape that does not show photoluminescence in the studied range. The excitation

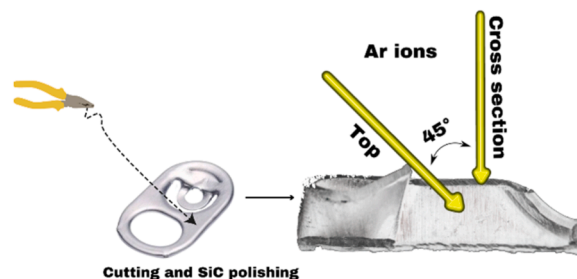


Fig. 1. Schema of the cross-section and top preparation for depth profile analysis by XPS using argon ions for sputtering.

wavelength was 254 nm, and the long-pass emission filters used were 270 and 325 nm. The optical reflectance of the pigment powder was measured using a UV-Vis-NIR spectrophotometer (Perkin Elmer Lambda 950, Waltham, MA, USA). As a baseline standard, BaSO₄ was used to measure the optical properties of the samples between 300 and 2500 nm. The NIR solar reflectance (R^*) of the pigments in the wavelength range of 750–2500 nm was obtained by the following Equation (1):

$$R_s = \frac{I_R}{I_0} = \frac{\int_0^{\infty} r_{\lambda} i_{\lambda,i} d\lambda}{\int_0^{\infty} i_{\lambda,i} d\lambda}$$

Where $r(\lambda)$ is the spectral reflectance obtained from the experimental, and $i(\lambda)$ is the spectral irradiance obtained from the standard of ASTM G173–03 reference spectra ($\text{W}\cdot\text{m}^{-2}\cdot\text{nm}^{-1}$).

2.2. Can seal characterization before recycling

The initial stage of the study involved the characterization of aluminum can seals. The seals were chosen due to their high aluminum content, low level of contaminants, and no requirement for pre-treatment to eliminate dyes, unlike whole cans. The X-ray diffractograms of the can seals indicate that they are predominantly composed of metallic aluminum (Fig. 2). However, low-intensity peaks (marked with arrows) attributed to magnesium oxide [33] are observed, which agrees with the results obtained from EDX and XPS.

EDX measurements of four can seals (reaction precursors) were performed at three points to verify their elemental composition (Table 1). The analysis revealed that the can seals are predominantly composed of aluminum (~76.6 at%), while carbon (~10.7 at%) and other impurities, such as magnesium, were also found in their composition. It is hypothesized that the carbon signal originates mainly from the sealant layer applied at the final stage of manufacturing the can seals. The sealant helps ensure perfect sealing, preventing leaks or loss of gas [17]; its composition usually consists of polyethylene (PE) and polypropylene (PP) polymers. These are flexible and resistant materials capable of forming an airtight seal. Fillers can be added to the sealant to improve its mechanical and processing properties. These fillers can include calcium carbonate, silica, or other inert materials. Additives are applied to provide specific characteristics to the sealant. For example,

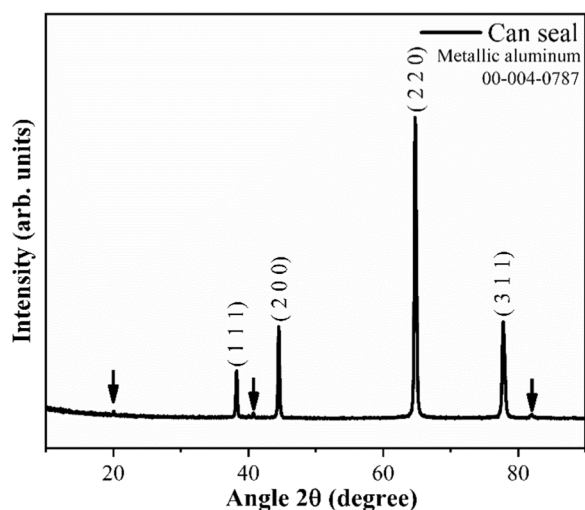


Fig. 2. Typical diffractogram of an aluminum can seal, indicating that the primary phase consists of metallic aluminum.

Table 1

The elemental concentration of four can seals evaluated by EDX. The EDX was recorded at three points of each seal.

Sample	Elements (%at)				
	Al	Mg	O	C	Cl
Can seal 1					
Point 1	74.9	3.9	9.4	11.7	0
Point 2	77.5	4.0	7.5	11.0	0
Point 3	79.8	3.9	7.0	9.3	0
Can seal 2					
Point 1	78.1	4.1	7.0	10.9	0
Point 2	79.6	4.0	6.5	9.8	0
Point 3	74.6	3.9	7.1	14.3	0
Can seal 3					
Point 1	82.3	4.1	6.4	7.3	0
Point 2	76.4	3.7	7.8	12.1	0
Point 3	81.3	3.5	7.0	8.2	0
Can seal 4					
Point 1	62.6	3.1	23.5	10.0	0.7
Point 2	73.6	3.5	9.9	13.0	0
Point 3	77.9	4.2	6.6	11.3	0
Average	76.6	3.8	8.8	10.7	~ 0

antioxidants can be added to protect the sealant from degradation caused by exposure to light or heat [34]. Other additives may include UV stabilizers, colorants, or lubricants. Some sealants may contain bonding agents to improve adhesion between the sealant and the surface of the aluminum can. These agents can be based on resins, silanes, or other chemical compounds. It is important to highlight that sealant formulations can vary between manufacturers and can be adapted to the specific requirements of each application [22]. However, exact sealant formulations are often proprietary information and, therefore, not publicly available.

To investigate the source of carbon in the elemental composition of the can seals, depth profile XPS measurements were performed, and the amount of aluminum and carbon were monitored (Fig. 3). Two geometries were explored for the sputtering: a depth profile from the top region and a cross-section exposing the bulk of the seal. In the depth profile performed from the top of the aluminum can seal, the relative atomic percentage of carbon decreases from 38% to 0% with increasing depth of analysis, indicating that carbon is mainly localized near the surface. This is confirmed when performing the depth profile in the cross-section cut where the sealant layer is absent. The atomic percentage of carbon dropped to zero after the first sputtering cycle. Thus, it is suggested that the carbon signal arises from the sealant layer on the surface.

Scanning electron microscopy was performed to evaluate the morphology of the can seals. Typical SEM micrographs are shown in Fig. S1 (See Supplementary Material). The micrographs reveal imperfections in the seal, probably caused by the manufacturing process or handling of the aluminum can. The SEM images recorded on the cross-section following a similar geometry as the XPS measurements show a smooth surface (Fig. S2). The cross-section cut was polished and analyzed using a backscattered electron detector (LABSE) to determine the thickness of the sealant layer present in the seal (Fig. 4). LABSE is a specific type of backscattered electron detector positioned at a low angle to the sample, allowing the detection of backscattered electrons scattered at small angles. This provides enhanced contrast for analyzing materials with different scattering properties. Exploring the contrast in the micrograph (Fig. 4a), the thin, darker layer can be associated with a carbon-containing layer, and a thicker, lighter layer is related to an aluminum layer. Fig. 4b presents the chemical mapping corresponding to the SEM micrograph, a thin layer of carbon represented in green and an extensive layer of aluminum represented in red. The thickness of the sealant layer is approximately ~65 nm, which is in accordance with the XPS depth profile (Fig. 3), which shows that at ~60 nm under the surface, the concentration of carbon is very low.

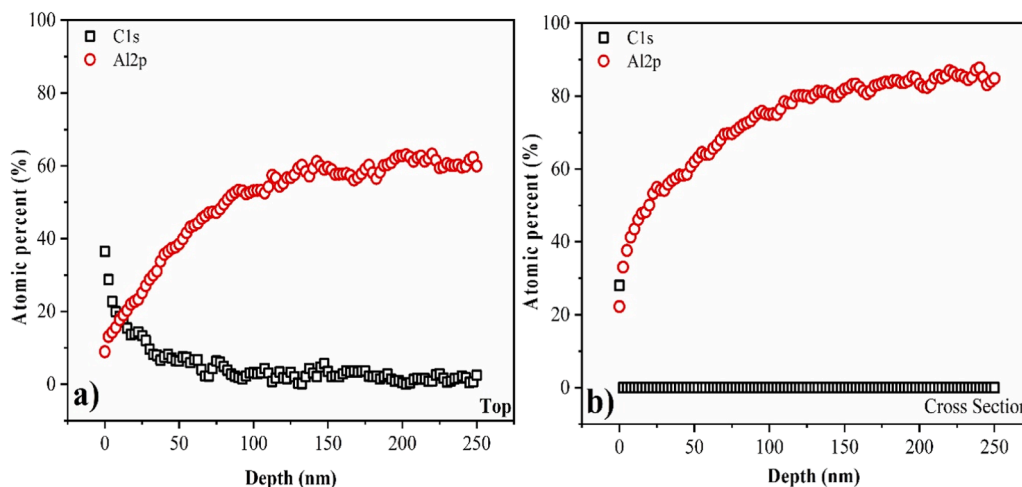


Fig. 3. XPS Depth profile of aluminum can seal made at the a) top of can seal and b) cross-section cut. The carbon is present primarily near the surface of the aluminum can seal.

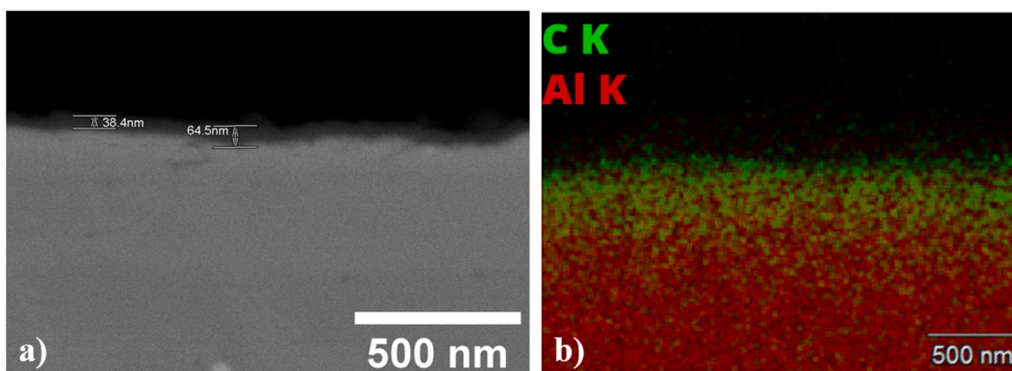


Fig. 4. a) Micrograph of the cross-section of the aluminum can seal using a backscattered electron detector (LABSE) and b) chemical mapping of the same region showing the elemental composition of the layers.

2.3. Can seal recycling – boehmite-like synthesis

The detailed characterized can seals were used for obtaining aluminum. First, the aluminum can seals were washed in running water to remove major contamination. Then, acid digestion of the can seals was performed using HCl in the proportion of 1 g of metallic aluminum for 100 mL of solution (1.1 mol L^{-1}) (Fig. 5). After obtaining the Al^{3+} ions in the solution, the pH was corrected to 8 with the addition of NaOH to precipitate the boehmite. Subsequently, the sample was filtered and dried. As NaCl is also formed during the reaction, a step for its removal is necessary. In this step, the powder in an aqueous medium was heated to its boiling point, exploiting the disparity in solubility between the NaCl

and the boehmite. Following a 5-minute boiling, the sample was vacuum-filtered using a Buchner funnel and dried at $70 \text{ }^\circ\text{C}$ for 24 hours [27].

3. Results and discussion

The recycled material is a white powder after a cleansing step, as shown in Fig. 5. We turn now to the comprehensive characterization of this powder using various techniques.

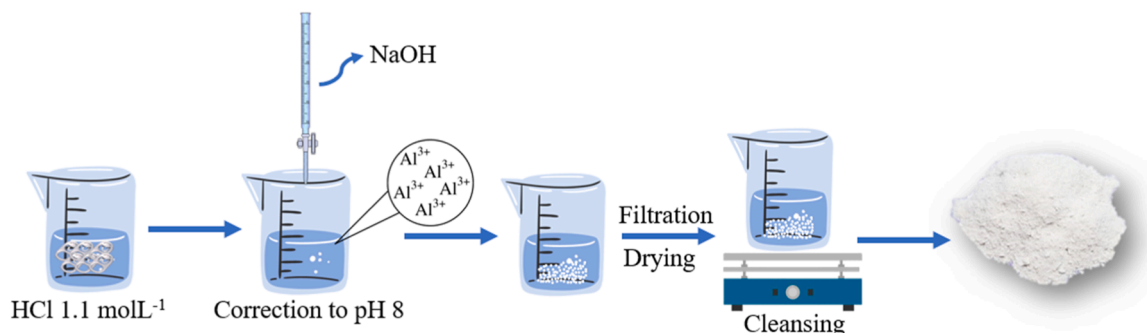


Fig. 5. Schematic representation of the synthesis process for boehmite-like.

3.1. Morphology by scanning electron microscopy (SEM)

Fig. 6 displays a micrograph revealing that the powder is composed of plate-like agglomerates. As discussed in the next section, the agglomerates have a boehmite-like crystallographic phase. The boehmite-like agglomerates particular morphology is a result of the precipitation synthesis route, whereby the precipitate particles exhibit minimal electronic charge, thereby promoting agglomeration [35]. In addition, it has been reported that the lower the synthesis temperature, the greater the tendency to form agglomerates [35]. The average size observed for the particles was $\sim 0.39 \mu\text{m}$ (Fig. 6b).

The elemental composition of the powder obtained by EDX is shown in Table 2. The presence of chlorine is attributed to the acid digestion process used to obtain Al^{3+} ions in the solution (Fig. 5). Sodium may remain from the NaOH used for precipitation, although its concentration is below EDX detection limit. Notably, the percentage of carbon (1.9 at %) in the powder is lower than that observed in the can seal by EDX (~ 10.7 at%), supporting the hypothesis that the sealant is the carbon source in the can seals. However, during the wash step the carbon that has been digested is leached out, and the remaining amount of carbon does not adversely affect the application as a precursor for synthetic inorganic pigments.

3.2. Crystallographic phase by X-ray diffractometry (XRD)

The observed crystallographic phase using XRD (Fig. 7) is similar to the boehmite phase RRUFF ID: R120123.9, thereby confirming the efficient synthesis route. However, the broad structures in the XRD pattern indicate a low degree of crystallinity. Therefore, the powder is classified as “boehmite-like”. This occurred due to the choice of pH used; according to the Pourbaix diagram [36], at pH 8, there is a predominance of $[\text{Al}(\text{OH})_4]^-$ species, favoring the preparation of the boehmite phase ($\text{AlO}(\text{OH})$) by dehydration. Typically, the boehmite phase precipitation occurs between pH 7 and 10 at temperatures ranging from 20°C to 85°C . The pH is a crucial synthesis parameter for obtaining the boehmite phase due to the difference in solubility of species (Al^{3+} , AlOH^{2+} , HAlO_2 , AlOH^{2-}) as a function of the pH [37]. In this work, the precipitation was carried out at room temperature ($\sim 25^\circ\text{C}$), and the pH was 8, minimizing energy consumption in the synthesis, different from what has been reported in the literature for the synthetic precipitation route that uses a higher temperature, i.e., $\sim 85^\circ\text{C}$ [35,38].

3.3. Boehmite-like thermogravimetric analysis

Fig. 8 shows the thermogravimetric analysis of the boehmite-like obtained through metallic aluminum recycling. The first event observed up to 100°C involves a mass loss of 18%. This can be attributed to the loss of water molecules between the boehmite-like layers and the elimination of water from the precipitated aluminum hydroxide

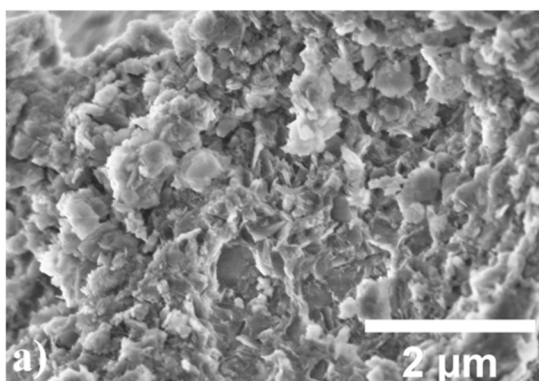


Table 2
Elemental composition obtained by EDX.

Sample	Elements at%			
	Al	O	Cl	C
Boehmite-like	25.6	69.9	2.5	1.9

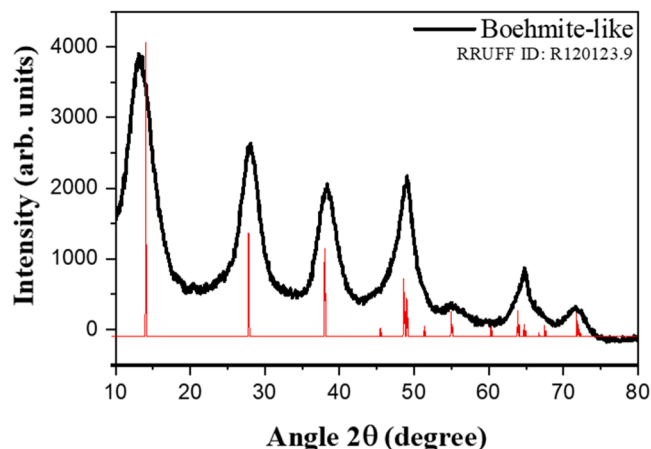


Fig. 7. XRD Diffractogram of the boehmite-like phase obtained by recycling metallic aluminum.

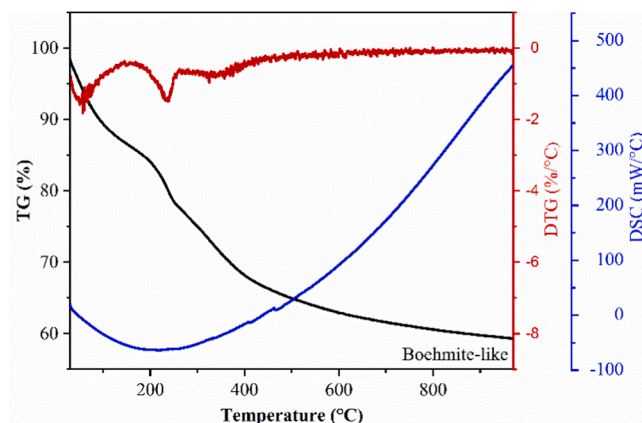


Fig. 8. TGA curves of boehmite-like were obtained by scanning from 30° to 1000°C in an oxygen atmosphere with a flow rate of 50 mL/min and a heating rate of 10°C/min .

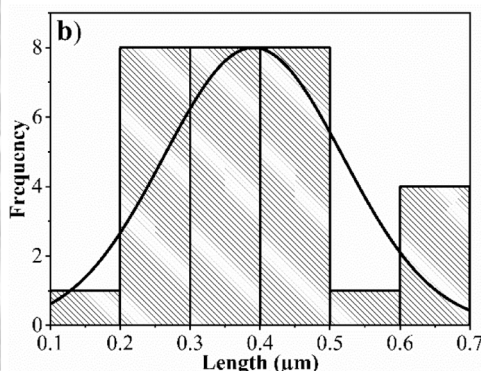


Fig. 6. a) Micrograph of the boehmite-like powder showing agglomerates b) boehmite-like particle size histogram.

hydrated [39,40]. From this temperature, the second main event occurs, with 14.5% mass loss up to approximately 420 °C, which can be attributed to the structural modification of the boehmite-like. This temperature is similar to the observed for the natural boehmite [41]. However, the literature reports the loss of hydroxyl groups at up to 550 °C for boehmite obtained via hydrolysis and precipitation with varied morphologies [40,42,43]. The decrease in the temperature required for structural modification may be attributed to the formation of smaller crystals resulting from the loss of hydroxyl groups and the transformation of the oxyhydroxide into alumina (γ -Al₂O₃) [39,44]. However, the dehydroxylation of natural boehmite occurs at similar temperatures. In contrast, the boehmite-like synthesized in this study, characterized by plate-like morphology, exhibits dehydroxylation at a lower temperature than previously observed, thus requiring less energy for crystallographic phase conversion.

3.4. Boehmite-like UV-Vis spectroscopy

The absorption spectrum is used to identify the wavelengths of light absorbed by a material, which can provide information about the chemical composition and structure. The boehmite-like absorption spectrum (Fig. 9a) shows a broad band centered at approximately 475 nm, possibly associated with the presence of NaCl in the sample, referring specifically to a single electron trapped in an anion vacancy, identified as F absorption [45]. Fig. 9b) presents the linear extrapolation of the curve obtained from the reflectance spectrum and represents the estimated value of the energy band gap (EBG) using the Kubelka-Munk method [46]. The energy band gap determines the electrical conductivity of a material and its ability to absorb or emit light. The band gap for the synthesized boehmite-like was ~3.7 eV. This value is lower than reported in the literature (~5.5 eV) [46,47], possibly due to defect-associated electronic states and also to particle size effects in the electronic states. It was reported that the boehmite band gap increases as the pH used for its synthesis increases because pH controls particle size [46]. In addition, plate-like agglomerates in a material can facilitate interlayer interactions, decreasing the distance between the valence and conduction bands. This is attributed to the stronger atom-to-atom interaction within the particles, mainly due to the incorporation of neighboring atoms in the layered structure. Consequently, the band gap value tends to decrease [46].

3.5. Boehmite-like photoluminescence

The boehmite-like photoluminescence spectrum showed a broad and intense band of blue emission centered at ~406 nm (Fig. 10). This can be attributed to anion vacancies from F and F+ centers or a combination

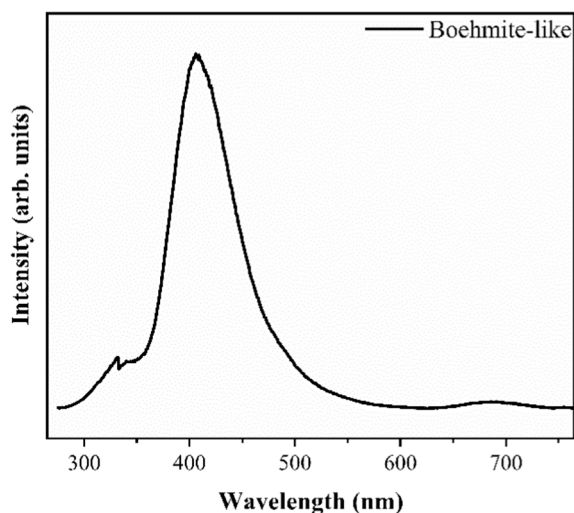


Fig. 10. Photoluminescence spectrum from boehmite-like obtained by recycling aluminum can seals. The PL blue emission band is centered at ~406 nm. The excitation wavelength was 254 nm. The jump at 325 nm is due to long-pass optical filter exchange.

of these defects [48]. The electronic transitions between the local band edge and the F+ center defects result in the photon emission from the F+ center in the visible blue wavelength region [49]. The F+ center corresponds to an oxygen vacancy with one electron, being positively charged with respect to the lattice, and the F center has two electrons and is electrically neutral with respect to the lattice [50]. Reports show a similar band with a maximum at 441 nm for boehmite synthesized using high-purity reagents, so the aluminum source alters the defects in the structure [48].

The blue emission observed in the boehmite-like is fundamental for producing white light in LEDs (light emitting diodes). Blue LEDs and luminescent phosphors that convert blue light into green and red light create long-lasting, efficient white light sources [51]. Blue emission forms colors and images in liquid crystal displays (LCDs) and OLED screens. The combination of different red, green, and blue light emissions creates a wide range of visible colors [52]. Materials that emit blue light can be used as markers or probes in various biological and chemical applications. For example, blue-emitting fluorescent dyes can be used in cell biology to label and track different cellular components [53]. In addition, blue-emitting semiconductors can be used as photodetectors, converting incident blue light into electrical signals [54], a possible application for the boehmite-like synthesized in this work since its band

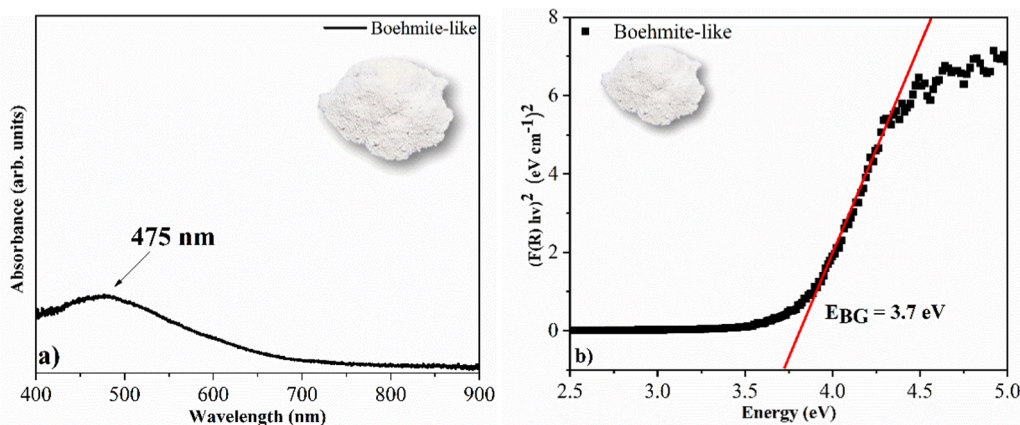


Fig. 9. a) Visible absorption spectrum of boehmite-like with a broad band centered at ~475 nm b) band gap energy estimation calculated by Kubelka-Munk method [46].

gap is ~ 3.7 .

4. Manganese aluminate pigment from recycled can seals

4.1. Synthesis

4.1.1. Brown pigment synthesis

In 50 mL of water, 5%, 10%, and 20% of MnCl_2 was added to the total mass of boehmite-like powder (w/w). Then, 3 g of boehmite-like were added and left under constant stirring (600 rpm) for 24 h. After this period, the mixture was calcined at 1000 °C, macerated, and stored. The samples were named $\text{MnAl}_2\text{O}_4 - 5$, $\text{MnAl}_2\text{O}_4 - 10$, and $\text{MnAl}_2\text{O}_4 - 20$.

4.1.2. Application as pigments

Water-based acrylic paint for outdoor and indoor was used to evaluate the use of manganese aluminates as pigments for architectural paints. 10 wt% of the colored powder to the total mass of acrylic white paint was dispersed in the proportion of 2:1 paint/water [27]. The prepared dispersion was applied on plaster specimens by painting two coats of paint according to the manufacturer's instructions.

4.1.3. Color stability test

The color stability test was carried out in acidic and alkaline environments using desiccators as a controlled experimental environment. A petri dish was placed in each desiccator with hydrochloric acid (HCl) and sodium hydroxide (NaOH), both $1 \text{ mol}\cdot\text{L}^{-1}$, to yield environments with aggressive vapors [55]. The plaster blocks were placed in the desiccators, which were then sealed. Colorimetric measurements were performed before the test and after 240 h to determine the colorimetric stability of the aluminates applied as synthetic inorganic pigments [26].

4.2. Results

4.2.1. Morphology analysis

The SEM micrographs show irregular agglomerates in the micrometer range for the different MnAl_2O_4 samples (5, 10, and 20) (Fig. 13). Reports suggest this is the typical morphology of manganese aluminate [56,57]; galaxite morphology can occur in granular aggregates or compact masses, without a well-defined crystalline form, with a massive and rock-like appearance [58]. The granular morphology of galaxite is beneficial for refractory applications and for promoting the uniform distribution of the material in coatings, helping to improve mechanical resistance and thermal stability in these materials.

4.2.2. Evaluation of the crystallographic phase

The sample prepared with manganese showed two phases: aluminum oxide $\alpha\text{-Al}_2\text{O}_3$ [96-900-8082] and Galaxite - MnAl_2O_4 [96-900-0877] (Fig. 11). The Galaxite phase has a typical spinel-like structure in which Mn^{2+} ions are strongly ordered at tetrahedral sites and is also known as manganese aluminate [59]. The coexistence of these two phases may result from variations in environmental conditions, such as temperature, causing the formation of distinct phases [60] related to the difference in Mn solubility within the $\alpha\text{-Al}_2\text{O}_3$ network. That is, due to the tendency of the Mn ion to spinel formation, low solubilization in the $\alpha\text{-Al}_2\text{O}_3$ phase is expected because the structure is more compact [61]. Combining alumina and galaxite phases can be advantageous in specific applications such as ceramic products, refractories, linings, and catalysis. The mixture can provide combined properties of wear resistance, temperature resistance, and electrical insulation, depending on the ratio in which they are mixed. In the case of this work, the properties of this mixture of phases in the NIR reflectance were studied.

4.2.3. Chemical characterization of the pigment

The chemical composition at the particles surface was studied using XPS (Table 3). The highest percentage of manganese (6.9 at%) was

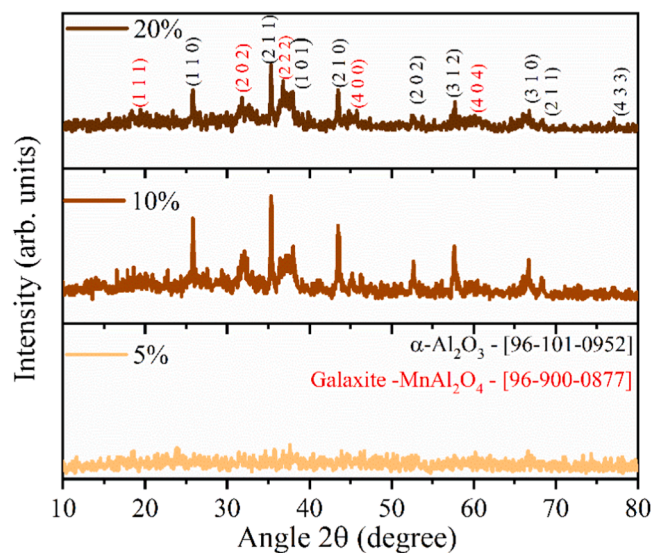


Fig. 11. The diffractogram of manganese aluminates in different percentages of added manganese. Indexing in black: $\alpha\text{-Al}_2\text{O}_3$ [96-101-0952] and in red: galaxite (MnAl_2O_4) [96-900-0877].

Table 3

Composition of the MnAl_2O_4 samples according to XPS.

Sample	Elements (at%)				
	Al	O	Mn	Na	Mg
$\text{MnAl}_2\text{O}_4 - 5$	29.5	63.2	3.0	3.6	0.8
$\text{MnAl}_2\text{O}_4 - 10$	26.7	63.5	6.9	2.3	0.7
$\text{MnAl}_2\text{O}_4 - 20$	27.2	61.7	6.7	3.4	0.9

observed in the $\text{MnAl}_2\text{O}_4 - 10$ sample, with the lowest sodium concentration (2.3 at%). The presence of sodium can be associated with residues of NaCl used in the boehmite-like preparation. The stability and durability of the pigments can be impacted by sodium chloride residues. NaCl is an ionic compound that can react with other compounds in the pigment or the environment. These reactions can lead to undesirable changes in the physical and chemical properties of the pigment, affecting its stability and durability [62]. For example, sodium chloride is hygroscopic. If a pigment containing sodium chloride is exposed to a humid environment, the salt can attract moisture, forming salt crystals and the pigment absorbing water. This can result in color changes, pigment agglutination, deformation, or deterioration of the support on which the pigment is applied, among other problems [63].

Furthermore, under certain circumstances, sodium chloride may react with other compounds in the pigment, such as binders or other additives, resulting in corrosive processes or chemical degradation. These reactions can lead to loss of color, changes in the crystalline structure of the pigment, or even the formation of unwanted chemicals. However, the percentage of NaCl observed for the pigments was low and could be removed with water wash cycle. Thus, the pigment $\text{MnAl}_2\text{O}_4 - 10$ is expected to show higher stability because it has the lowest percentage of NaCl. In addition, the EDX analysis did not reveal the presence of sodium and chlorine contamination within the bulk of the particles, suggesting that contamination is at their surface.

The XPS Mn 2p core level spectra for the MnAl_2O_4 samples are shown in Fig. 12 a). The satellites are particularly sensitive to the stoichiometry of the aluminate, decreasing in relative intensity upon either surface oxidation or reduction and disappearing completely in higher oxide phases [64], suggesting the $\text{MnAl}_2\text{O}_4 - 5$ sample is mainly composed of oxide and not aluminate, as seen on the XRD pattern. The Mn 3s peaks indicate that the aluminate structure is rich in Mn^{2+} ions (Fig. 12b)), which is confirmed by the peak splitting of 5.9 eV [65]. This split is

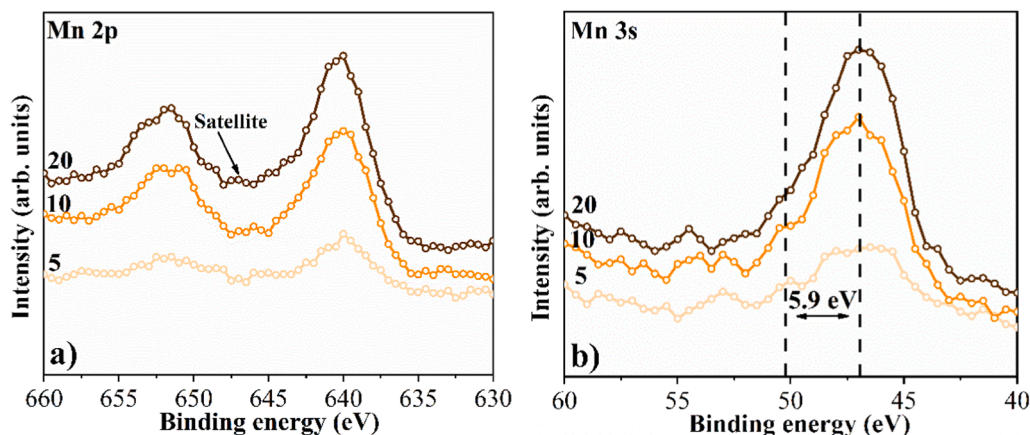


Fig. 12. XPS of the MnAl_2O_4 samples a) Mn 2p and b) Mn 3s core level spectra. The satellite feature is indicated with an arrow.

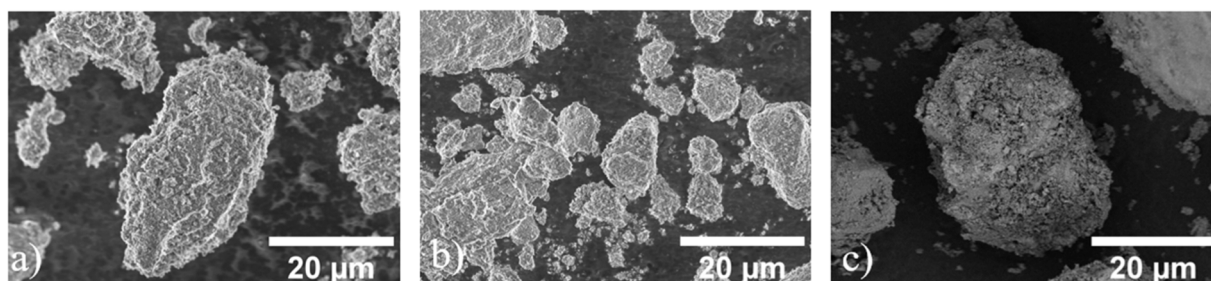


Fig. 13. SEM micrographs of the manganese aluminates ($20\ \mu\text{m}$) samples: a) $\text{MnAl}_2\text{O}_4 - 5$, b) $\text{MnAl}_2\text{O}_4 - 10$, and c) $\text{MnAl}_2\text{O}_4 - 20$. The morphology does not vary in the Mn concentration range studied.

caused by an interaction between the electrons in the d orbitals of manganese and the crystal field in which it is embedded, characteristic of the presence of Mn^{2+} .

4.2.4. Absorbance

Manganese aluminate does not have significant optical properties in the visible absorption spectrum (Vis) (Fig. 14); being an opaque or semi-transparent powder, it does not show distinct absorption or transmission in this wavelength range. The UV-Vis spectrum is commonly used to

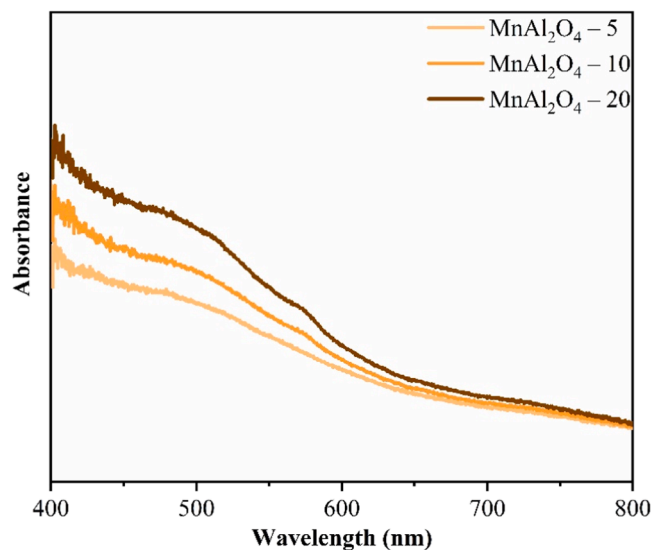


Fig. 14. The absorption spectrum in the visible region of manganese aluminates. The spectra have a broad band centered at $\sim 510\ \text{nm}$.

analyze the light absorption by substances at different wavelengths. However, in the case of galaxite, light cannot pass through the material due to its opacity, and no specific absorption in the Vis spectrum can be attributed to it.

The broad band observed at $\sim 510\ \text{nm}$ in the absorption spectrum was attributed to the ${}^4\text{T} \rightarrow {}^6\text{A}({}^6\text{S})$ transition of Mn^{2+} [66], which is a high-spin to low-spin transition. In spectroscopic terms, ${}^4\text{T}$ refers to a term with a spin multiplicity of 4 (tetraquartet), while ${}^6\text{A}({}^6\text{S})$ denotes a term with a spin multiplicity of 6 (hexasextet) and with the contribution of the orbital 6s. Transitions from high to low spin are common in transition metal ion systems. These transitions involve the redistribution of electrons between orbitals of different energies, usually from d orbitals to p orbitals. A change in electron configuration and orbital occupation occurs during the transition from high to low spin. The energy difference between the two electronic states corresponds to the energy released or absorbed in this transition. Each transition system and ion has its characteristics and behaviors, which can result in different observed electronic transitions [67]. The observation of Mn^{2+} agrees with the XPS results, indicating that the obtained manganese aluminate is rich in Mn^{2+} ions in the galaxite phase observed by XRD. These Mn^{2+} ions are responsible for imparting the brown color to the pigment.

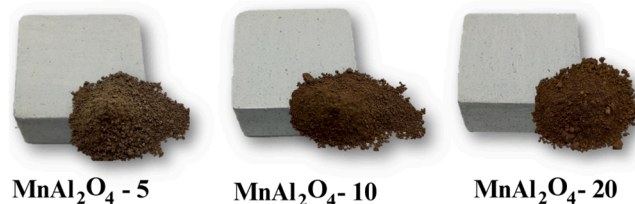


Fig. 15. Photographic image of manganese aluminates in powder form and after its dispersion in white commercial paint and applications in plaster blocks.

4.2.5. Colorimetry

The pigments are brown before and after dispersion and application (Fig. 15). Brown is a tertiary color usually associated with earthy and natural tones, and it plays an essential role in conveying feelings of connection to nature, stability, authenticity, elegance, and versatility. It adds depth, warmth, and a sense of visual balance to objects and places dispersion in white acrylic paint and application on plaster surfaces.

The CIEL*a*b* color model comprises three components: L*, a*, and b*. These components represent luminosity (L*), position on the red-green axis (a*), and position on the yellow-blue axis (b*). The value of L* ranges from 0 (black) to 100 (white), while the values of a* and b* range from -128–127 [68]. In Table 4, it is possible to observe that all samples have positive values for both a* and b*. Therefore, they are arranged in the red/yellow quadrant (Fig. 16). C* chromaticity is used to describe the intensity or saturation of the color. It represents the distance between a point in the L*a*b* color space and the lightness axis (L*) [68]. In this work, the chromaticity increases as the percentage of coloring ion (Mn) increases, confirming that the color depends directly on the coloring ion both in hue and saturation.

4.2.6. Color stability

After dispersion in a commercial water-based acrylic white paint and application on a plaster surface, the color stability of the pigments in aggressive environments (acid and alkaline) with an exposure of 240 h was evaluated. The total color difference (ΔE) was calculated by comparing no exposed and exposed samples synthesized with the same parameters (Table 5). Total color difference (ΔE) is a measure used to quantify the color difference between two samples or colors. A total color difference (ΔE) value close to zero indicates a close match or an unnoticeable color difference. The higher the ΔE value, the greater the color difference between the samples. Generally, a ΔE less than one is considered an imperceptible difference, while a ΔE above 3 or 4 can be easily discernible to the human eye [69]. The white (commercial water-based acrylic) paint was exposed to the same environments for the same amount of time. In both environments, the sample that presented the best performance (smallest color difference, higher stability) was the sample MnAl₂O₄ - 10, showing that the percentage of 10% manganese (Mn) and less amount of sodium led to the most stable sample against aggressive environments. However, the values obtained were generally low and close to 1, i.e., the color variation is nearly imperceptible to the human eye.

4.2.7. NIR reflectance

Heat reflectance is an essential characteristic of architectural paints for mitigating urban heat island effects. In this context, the NIR reflectance of the MnAl₂O₄ - 10, the most stable sample, is shown in Fig. 17. The bands in the NIR spectrum associated with the Mn²⁺ ion are related to electronic transitions between the energy levels of the d electrons of manganese due to the crystal field around it. The solar reflectance (R*) in the wavelength range of 780–2500 nm was calculated according to the standard ASTM E 891–87 [70], as described in the literature [71]. The value of R is determined by equation (1):

Table 4
Colorimetric parameters of manganese aluminates in powder form.

Sample	Colorimetric Parameters				
	L*	a*	b*	C*	h*
MnAl ₂ O ₄ - 5	35.5	5.8	11.7	13.1	63.8
MnAl ₂ O ₄ - 10	34.0	9.4	12.1	15.4	52.1
MnAl ₂ O ₄ - 20	36.5	14.6	13.3	19.8	42.2

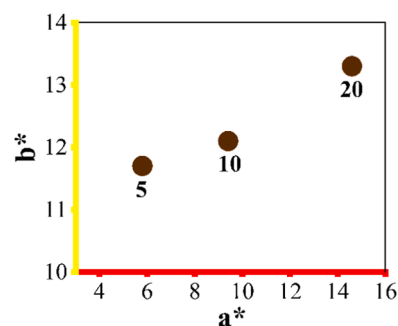


Fig. 16. Graph of the chromatic parameters (a versus b) of the manganese aluminates, indicating that all samples are in the same red/yellow color quadrant.

$$R_s = \frac{I_R}{I_0} = \frac{\int_0^{\infty} r_{\lambda} i_{\lambda} d\lambda}{\int_0^{\infty} i_{\lambda} d\lambda}$$

where $r(\lambda)$ is the experimentally obtained spectral reflectance ($W m^{-2}$) and $I(\lambda)$ is the solar spectral irradiance ($W m^{-2} nm^{-1}$) obtained from ASTM standard E891–87 [71].

Based on the emission spectra for the NIR and the typical Mn²⁺ absorbance spectrum in MnAl₂O₄ (Fig. 14), the NIR emission cannot be attributed to the other valence states of Mn (such as Mn³⁺, Mn⁴⁺, Mn⁵⁺, or Mn⁶⁺). The similar excitation spectra for the VIS and NIR emissions indicate that the NIR emission should also be related to the Mn²⁺ [72]. Due to the interaction with the crystal field around the Mn²⁺ ion, the d-d transitions occur over a wide range of energies, resulting in broad bands in the NIR [73].






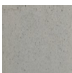
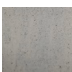

Reports show that the near-infrared (NIR) reflectance of other brown pigments, such as the iron chocolate brown pigment (R* = 33%) and the dark brown BiFeO₃ pigment (R* = 43%), is lower than the NIR reflectance obtained in this study (R* = 50%) [65]. Thus, it can be inferred that the pigment MnAl₂O₄ - 10 exhibits higher efficiency in absorbing minimal solar heat, thereby reducing heat in environments where surfaces are exposed to direct sunlight. As a result, the MnAl₂O₄-10 pigment can potentially decrease cooling loads on buildings, ultimately reducing energy consumption required to maintain comfortable indoor temperatures.

5. Conclusion

In conclusion, our study demonstrated the successful recycling of aluminum can seals to produce a boehmite-like precursor for synthesizing an inorganic brown pigment. The characterization of the aluminum can seal revealed the presence of a coating containing mainly carbon at the can seal surface associated with a finishing sealant. The proposed sustainable synthetic route used to obtain boehmite-like was efficient. The obtained boehmite-like powder has a lower dihydroxylation temperature than reported in the literature, making it a good precursor for alumina due to the lower energy needed for the phase transformation. The synthesized material also showed promising thermal stability and optical properties, making it suitable for various applications, such as liquid crystal displays, biological markers, and photodetectors. Furthermore, our X-ray diffraction analysis confirmed the successful transformation of boehmite-like to galaxite phase manganese aluminate. The pigment synthesized from this material showed excellent color stability in aggressive environments, with the MnAl₂O₄ - 10 sample having the most stable color. The evaluation of color stability was associated with a lower amount of sodium chloride in its

Table 5

Colorimetric parameters of the plaster surface painted with the commercial water-based acrylic white paint pigmented with manganese aluminates after 240 h of exposure to aggressive environments. Photography of the painted surfaces, the color difference before and after exposure is nearly imperceptible to the human eye.

Environment	Sample	Colorimetric Parameters						Photo
		L*	a*	b*	C*	h*	ΔE	
Acid	White paint – 240 h	96.8	0.4	1.2	1.3	71.3	1.3	
	5– 240 h	81.2	2.9	5.8	6.6	64.0	1.2	
	10– 240 h	80.4	3.0	4.6	5.5	57.1	0.9	
	20– 240 h	77.4	3.7	5.3	6.5	55.5	1.6	
Alkali	White paint – 240 h	95.6	0.3	1.0	1.1	73.3	0.9	
	5– 240 h	80.8	2.5	5.3	5.8	65.0	1.2	
	10– 240 h	79.5	3.1	5.2	6.1	59.1	0.7	
	20– 240 h	76.7	3.7	5.3	6.5	55.1	1.0	

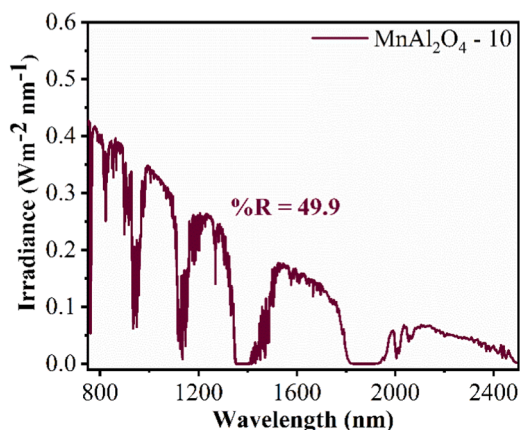


Fig. 17. NIR solar reflectance spectrum of the $\text{MnAl}_2\text{O}_4 - 10$ sample.

composition. Our investigation also revealed that the pigment obtained via can seal recycling has high near-infrared reflectance, making it an option for interior and exterior applications. Our study provides a promising alternative for sustainable pigment production and recycling of aluminum can seals.

Supporting information

Supporting Information File 1: [Fig. S1](#): micrographs of the top of the polished cross-section cut of aluminum can seal at different magnifications; [Fig. S2](#): Micrographs of the can seal before polishing and cross-

section (can seal untreated) at different magnitudes.

Funding

D. F. L. H. thanks the Coordenação de Aperfeiçoamento de Pessoal de Nível Superior-Brasil (CAPES) – Finance Code 001 for a graduate scholarship, D. F. L. H. thanks UMONS for the Ph.D. grant, J. d. O. P. thanks the FNRS for the mobility grant (2021/V6/5/003-JG/MF-726). C. B. is a Research Associate of the FRS-FNRS, Belgium. C. B. and J. P. thank the Belgian Fund for Scientific Research under the FRFC contract EQP 40002995 (PHOTOFUN). F. J. A. is thankful for a CNPq Productivity grant (308625/2019-6) and the grants CNPq-427127/2018-1 and Fundação Araucária-CBPA-001/2016 project NARROWW (CONFAP-WBI).

Declaration of Competing Interest

The authors declare that they have no known competing financial interests or personal relationships that could have appeared to influence the work reported in this paper.

Acknowledgements

The authors thank Lisa Dangreau and Alice Belfiore for the SEM analysis and Diego F. L. Horsth for help with image processing.

Appendix A. Supporting information

Supplementary data associated with this article can be found in the online version at [doi:10.1016/j.nxsust.2023.100009](https://doi.org/10.1016/j.nxsust.2023.100009).

References

- [1] Y. Liu, D. Ma, X. Han, X. Bao, W. Frandsen, D. Wang, D. Su, Hydrothermal synthesis of microscale boehmite and gamma nanoleaves alumina, *Mater. Lett.* 62 (2008) 1297–1301, <https://doi.org/10.1016/j.matlet.2007.08.067>.
- [2] I.S. Park, M.S. Kwon, N. Kim, J.S. Lee, K.Y. Kang, J. Park, Rhodium nanoparticles entrapped in boehmite nanofibers: recyclable catalyst for arene hydrogenation under mild conditions, *Chem. Commun.* (2005) 5667–5669, <https://doi.org/10.1039/b511577a>.
- [3] D.F.L. Horsth, J. de O. Primo, N. Balaba, J.S. Correa, C.M. Zanette, D.K. Silva, C. Bittencourt, F.J. Anaissi, Synthesis and characterization of boehmite particles obtained from recycling: water disinfection application, *Nanomaterials* 12 (2022) 2771, <https://doi.org/10.3390/nano12162771>.
- [4] F. Granados-Correa, J. Jiménez-Becerril, Chromium (VI) adsorption on boehmite, *J. Hazard Mater.* 162 (2009) 1178–1184, <https://doi.org/10.1016/j.jhazmat.2008.06.002>.
- [5] M. Mohammadi, M. Khodamorady, B. Tahmasbi, K. Bahrami, A. Ghorbani-Choghmarani, Boehmite nanoparticles as versatile support for organic–inorganic hybrid materials: synthesis, functionalization, and applications in eco-friendly catalysis, *J. Ind. Eng. Chem.* 97 (2021) 1–78, <https://doi.org/10.1016/j.jiec.2021.02.001>.
- [6] S.J. Wilson, 1979. The Dehydration of Boehmite, γ -AlOOH, to γ -Al₂O₃, 1979.
- [7] E. Peigné, A. Poulon-Quintin, M. Cavarroc, G. Aubert, M. Duttine, C.L. Sarroste, C. Aymonier, Investigation of the interaction between adsorbed water and various morphologies of boehmite nanoparticles prepared by continuous supercritical hydrothermal synthesis, *J. Supercrit. Fluids* 193 (2023), 105829, <https://doi.org/10.1016/j.supflu.2022.105829>.
- [8] T. van Truong, D.J. Kim, Synthesis of high quality boehmite and γ -alumina for phosphorus removal from water works sludge by extraction and hydrothermal treatment, *Environ. Res.* 212 (2022), <https://doi.org/10.1016/j.envres.2022.113448>.
- [9] F. He, W. Li, T. Pang, L. Zhou, C. Wang, H. Liu, M. Li, X. He, Hydrothermal synthesis of boehmite nanorods from alumina sols, *Ceram. Int.* 48 (2022) 18035–18047, <https://doi.org/10.1016/j.ceramint.2022.02.212>.
- [10] M. Nguefack, A.F. Popa, S. Rossignol, C. Kappenstein, Preparation of alumina through a sol-gel process, synthesis, characterization, thermal evolution and model of intermediate boehmite, *Phys. Chem. Chem. Phys.* 5 (2003) 4279–4289, <https://doi.org/10.1039/b306170a>.
- [11] S.M. Kim, Y.J. Lee, K.W. Jun, J.Y. Park, H.S. Potdar, Synthesis of thermo-stable high surface area alumina powder from sol-gel derived boehmite, *Mater. Chem. Phys.* 104 (2007) 56–61, <https://doi.org/10.1016/j.matchemphys.2007.02.044>.
- [12] W. Jiao, X. Wu, T. Xue, G. Li, W. Wang, Y. Wang, Y. Tang, M.Y. He, Morphological controlled growth of nanosized boehmite with enhanced aspect ratios in an organic additive-free cationic-anionic double hydrolysis method, *Cryst. Growth Des.* 16 (2016) 5166–5173, <https://doi.org/10.1021/acs.cgd.6b00723>.
- [13] J.T. Klopogge, H.D. Ruan, R.L. Frost, Thermal decomposition of bauxite minerals: infrared emission spectroscopy of gibbsite, boehmite and diaspore, *J. Mater. Sci.* 37 (2002) 1121–1129, <https://doi.org/10.1023/A:1014303119055>.
- [14] X. Wu, B. Zhang, Z. Hu, Microwave hydrothermal synthesis of boehmite hollow microspheres, *Mater. Lett.* 73 (2012) 169–171, <https://doi.org/10.1016/j.matlet.2012.01.050>.
- [15] R. Cao, L. Zhu, H. Liu, W. Li, Electrodeposition and hydrothermal transition of alumina sol film on sintered NdFeB magnets, *Surf. Coat. Technol.* 309 (2017) 820–828, <https://doi.org/10.1016/j.surfcoat.2016.10.079>.
- [16] S.G. Castellanos, V.V.A. Fernández, J. Aguilar, F.J. Moscoso-Sánchez, I. Ceja, G. Canché-Escamilla, A. Barrera, Synthesis and characterization of poly(methyl methacrylate)-boehmite nanocomposites by direct microemulsion polymerization combined with the in-situ sol-gel method, *Polymer* 163 (2019) 134–143, <https://doi.org/10.1016/j.polymer.2018.12.053>.
- [17] D. Panias, A. Krestou, Effect of synthesis parameters on precipitation of nanocrystalline boehmite from aluminate solutions, *Powder Technol.* 175 (2007) 163–173, <https://doi.org/10.1016/j.powtec.2007.01.028>.
- [18] A. Abdulkadir, A. Ajayi, M.I. Hassan, Evaluating the Chemical Composition and the Molar Heat Capacities of a white Aluminum Dross. *Energy Procedia*, Elsevier Ltd, 2015, pp. 2099–2105, <https://doi.org/10.1016/j.egypro.2015.07.326>.
- [19] P.E. Tsakiridis, P. Oustadakis, S. Agatzini-Leonardou, Aluminium recovery during black dross hydrothermal treatment, *J. Environ. Chem. Eng.* 1 (2013) 23–32, <https://doi.org/10.1016/j.jece.2013.03.004>.
- [20] M. Mahinroosta, A. Allahverdi, Hazardous aluminum dross characterization and recycling strategies: a critical review, *J. Environ. Manag.* 223 (2018) 452–468, <https://doi.org/10.1016/j.jenvman.2018.06.068>.
- [21] ABRALATAS, 2022. (<https://www.abralatas.org.br/>) (Accessed May 19, 2023).
- [22] H. Kvande, The aluminum smelting process, *J. Occup. Environ. Med.* 56 (2014) S2–S4, <https://doi.org/10.1097/JOM.0000000000000154>.
- [23] P.E. Tsakiridis, Aluminium salt slag characterization and utilization - A review, *J. Hazard Mater.* (2012) 217–218, <https://doi.org/10.1016/j.jhazmat.2012.03.052>, 1–10.
- [24] D.F.L. Horsth, M. Dalpasquale, F.J. Anaissi, Transformação de alumínio metálico em hidróxido de alumínio (Al(OH)₃) Uma ação para o desenvolvimento sustentável, *Braz. J. Dev.* 6 (2020) 34178–34190, <https://doi.org/10.34117/bjdv6n6-097>.
- [25] European Aluminium, 2022. (<https://european-aluminium.eu/>) (Accessed May 19, 2023).
- [26] D.F.L. Horsth, J. de O. Primo, N. Balaba, F.J. Anaissi, C. Bittencourt, Color stability of blue aluminates obtained from recycling and applied as pigments, *RSC Sustain.* 1 (2023) 159–166, <https://doi.org/10.1039/D2SU00057A>.
- [27] D.F.L. Horsth, J.O. Primo, M. Dalpasquale, C. Bittencourt, F.J. Anaissi, Colored aluminates pigments obtained from metallic aluminum waste, an opportunity in the circular economy, *Clean. Eng. Technol.* 5 (2021), <https://doi.org/10.1016/j.clet.2021.100313>.
- [28] N. Khaidukov, A. Pirri, M. Brekhovskikh, G. Toci, M. Vannini, B. Patrizi, V. Makhov, Time- and temperature-dependent luminescence of manganese ions in ceramic magnesium aluminum spinels, *Materials* 14 (2021) 1–13, <https://doi.org/10.3390/ma14020420>.
- [29] A.M. Arabi, S.J. Moeen, Solution Combustion Synthesis of MnAl₂O₄ Brown Pigments Using Different Fuel Mixtures, 2022. (www.pccc.icrc.ac.ir).
- [30] P.L. Edwards, Magnetic properties of the manganese chromite-aluminates, *Phys. Rev.* 116 (1959) 294–300, <https://doi.org/10.1103/PhysRev.116.294>.
- [31] M. Peng, X. Yin, P.A. Tanner, C. Liang, P. Li, Q. Zhang, J. Qiu, Orderly-layered tetravalent manganese-doped strontium aluminate Sr₄Al₁₄O₂₅:Mn⁴⁺: an efficient red phosphor for warm white light emitting diodes, *J. Am. Ceram. Soc.* 96 (2013) 2870–2876, <https://doi.org/10.1111/jace.12391>.
- [32] A. Morales-Marin, J.L. Ayastuy, U. Iriarte-Velasco, M.A. Gutiérrez-Ortiz, Nickel aluminate spinel-derived catalysts for the aqueous phase reforming of glycerol: effect of reduction temperature, *Appl. Catal. B* 244 (2019) 931–945, <https://doi.org/10.1016/j.apcatb.2018.12.020>.
- [33] R. López-Juárez, N. Razo-Perez, T. Pérez-Juace, O. Hernandez-Cristobal, S. Y. Reyes-López, Synthesis of α -Al₂O₃ from aluminum cans by wet-chemical methods, *Results Phys.* 11 (2018) 1075–1079, <https://doi.org/10.1016/j.rinp.2018.11.037>.
- [34] A. Adrados, I. de Marco, B.M. Caballero, A. López, M.F. Laresgoiti, A. Torres, Pyrolysis of plastic packaging waste: a comparison of plastic residuals from material recovery facilities with simulated plastic waste, *Waste Manag.* 32 (2012) 826–832, <https://doi.org/10.1016/j.wasman.2011.06.016>.
- [35] L. Rajabi, A.A. Derakhshan, Room temperature synthesis of boehmite and crystallization of nanoparticles: effect of concentration and ultrasound, *Sci. Adv. Mater.* 2 (2010) 163–172, <https://doi.org/10.1166/sam.2010.1063>.
- [36] Atlas of Eh-pH diagrams Intercomparison of thermodynamic databases, 2005.
- [37] K. Okada, T. Nagashima, Y. Kameshima, A. Yasumori, T. Tsukada, Relationship between formation conditions, properties, and crystallite size of boehmite, *J. Colloid Interface Sci.* 253 (2002) 308–314, <https://doi.org/10.1006/jcis.2002.8535>.
- [38] B. Dash, B.C. Tripathy, I.N. Bhattacharya, S.C. Das, C.R. Mishra, B.S. Pani, Effect of temperature and alumina/caustic ratio on precipitation of boehmite in synthetic sodium aluminate liquor, *Hydrometallurgy* 88 (2007) 121–126, <https://doi.org/10.1016/j.hydromet.2007.02.011>.
- [39] S. Zanganeh, A. Kajbafvala, N. Zanganeh, M.S. Mohajerani, A. Lak, M.R. Bayati, H. R. Zargar, S.K. Sadrnezhad, Self-assembly of boehmite nanoparticles to form 3D high surface area nanoarchitectures, *Appl. Phys. A Mater. Sci. Process* 99 (2010) 317–321, <https://doi.org/10.1007/s00339-009-5534-2>.
- [40] D.K. Trukhinov, E.A. Lebedeva, S.A. Astaf'eva, A.Sh Shamsutdinov, E. V. Kornilitsina, M. Balasoiu, Seed-assisted hydrothermal fabrication of nanostructured boehmite coating on carbon fiber, *Surf. Coat. Technol.* 452 (2023), 129083, <https://doi.org/10.1016/j.surfcoat.2022.129083>.
- [41] C.M.R. Prado, M.I.R. Alves, M.I.G. Leles, R.I. Medeiros, C.R.N. Otto, F. C. Damasceno, C.H.H. Brait, P.L.B.M. Franco, N.R. Antoniosi Filho, Estudo da ativação ácida e tratamento térmico de bauxita extraída de jazidas em Minas Gerais, *Brasil, Cerâmica* 58 (2012) 111–117.
- [42] S. Gundekari, K. Srinivasan, In situ generated Ni(O)₂/boehmite from NiAl-LDH: An efficient catalyst for selective hydrogenation of biomass derived levulinic acid to γ -valerolactone, *Catal. Commun.* 102 (2017) 40–43, <https://doi.org/10.1016/j.catcom.2017.08.020>.
- [43] G. Li, R.L. Smith, H. Inomata, K. Arai, 2002. Synthesis and thermal decomposition of nitrate-free boehmite nanocrystals by supercritical hydrothermal conditions, 2002. www.elsevier.com/locate/matlet.
- [44] R. Tettenhorst, D.A. Hofmann, 1980. CRYSTAL CHEMISTRY OF BOEHMITE, 1980.
- [45] T. Kurobori, W. Zheng, Y. Miyamoto, H. Nanto, T. Yamamoto, The role of silver in the radiophotoluminescent properties in silver-activated phosphate glass and sodium chloride crystal, *Opt. Mater.* 32 (2010) 1231–1236, <https://doi.org/10.1016/j.optmat.2010.04.004>.
- [46] M. Ghamari, G. Farzi, Effect of morphology control on optical properties of PMMA/boehmite nano-hybrid prepared through facile one-pot process, *J. Mater. Sci.: Mater. Electron.* 28 (2017) 16570–16574, <https://doi.org/10.1007/s10854-017-7570-6>.
- [47] S. Roy, A. Maity, P. Mandal, D.K. Chanda, K. Pal, S. Bardhan, S. Das, Effects of various morphologies on the optical and electrical properties of boehmite nanostructures, *CrystEngComm* 20 (2018) 6338–6350, <https://doi.org/10.1039/c8ce01171k>.
- [48] G. Rani, Photoluminescence characterizations in phase transition alumina with boehmite nanostructures, *J. Korean Ceram. Soc.* 58 (2021) 747–752, <https://doi.org/10.1007/s43207-021-00151-3>.
- [49] G. Gopal Khan, A.K. Singh, K. Mandal, Structure dependent photoluminescence of nanoporous amorphous anodic aluminium oxide membranes: role of F⁺ center defects, *J. Lumin.* 134 (2013) 772–777, <https://doi.org/10.1016/j.jlumin.2012.06.050>.
- [50] J.L. Park, Y. Chen, G.P. Williams, R.T. Williams, G.J. Pogatschnik, Luminescence of F⁺ centers in Cao crystals under pulsed-laser excitation, n.d.
- [51] P. Zhong, G. He, M. Zhang, S. Hattar, H.W. Liao, M. Takao, D.M. Berson, K.W. Yau, 2012. Spectral optimization of the color temperature tunable white light-emitting diode (LED) cluster consisting of direct-emission blue and red LEDs and a diposphor conversion LED References and links, 2012.

- [52] C. Zheng, P. Xiong, M. Peng, H. Liu, Discovery of a novel rare-earth free narrow-band blue-emitting phosphor $Y_3Al_2Ga_3O_{12}:Bi^{3+}$ with strong NUV excitation for LCD LED backlights, *J. Mater. Chem. C Mater.* 8 (2020) 13668–13675, <https://doi.org/10.1039/d0tc02720k>.
- [53] S. Ghorai, I. Roy, S. De, P.S. Dash, A. Basu, D. Chattopadhyay, Exploration of the potential efficacy of natural resource-derived blue-emitting graphene quantum dots in cancer therapeutic applications, *N. J. Chem.* 44 (2020) 5366–5376, <https://doi.org/10.1039/c9nj06239d>.
- [54] X. Xie, J. Zhao, O. Lin, Z. Yin, X. Li, Y. Zhang, A. Tang, Narrow-bandwidth blue-emitting Ag-Ga-Zn-S semiconductor nanocrystals for quantum-dot light-emitting diodes, *J. Phys. Chem. Lett.* 13 (2022) 11857–11863, <https://doi.org/10.1021/acs.jpcclett.2c03437>.
- [55] L.C.B. Lima, F.C. Silva, E.C. Silva-Filho, M.G. Fonseca, G. Zhuang, M. Jaber, Saponite-anthocyanin derivatives: the role of organoclays in pigment photostability, *Appl. Clay Sci.* 191 (2020), <https://doi.org/10.1016/j.clay.2020.105604>.
- [56] J.H. Park, D.J. Kim, D.J. Min, Characterization of non-metallic inclusions in high-manganese and aluminum-alloyed austenitic steels, *Met. Mater. Trans. A Phys. Met. Mater. Sci.* 43 (2012) 2316–2324, <https://doi.org/10.1007/s11661-012-1088-6>.
- [57] R. Dekkers, B. Blanpain, P. Wollants, STEEL SAMPLING TO STUDY INCLUSIONS, n.d.
- [58] N. Timoleon, G. Sylvestre, G.D. Kouankap Nono, N.J. Paul, Mineralogy and geochemistry of Neoproterozoic siliceous manganese formations from Ntui–Betamba (Cameroon Pan-African Fold Belt): implications for mineral exploration, *Int. J. Earth Sci.* 104 (2015) 1123–1138, <https://doi.org/10.1007/s00531-015-1157-3>.
- [59] H.S. Firozeh, A. Shafiekhani, A. Beheshti- Marnani, M.B. Askari, Synthesis of galaxite, $Mn_0.9Co_0.1Al_2O_4$, and its applications a novel nanocatalyst for electrochemical hydrogen evolution reaction, *Phys. B Condens Matter* 538 (2018) 172–178, <https://doi.org/10.1016/j.physb.2018.03.044>.
- [60] L.B. Kong, J. Ma, H. Huang, $MgAl_2O_4$ spinel phase derived from oxide mixture activated by a high-energy ball milling process, 1100. (www.elsevier.com/locate/matlet).
- [61] H.H.E. Dörre, *Alumina Processing, Properties, and Applications*, Springer-Verlag, Berlin, 1984.
- [62] A. Kalendová, D. Veselý, J. Stejskal, Organic coatings containing polyaniline and inorganic pigments as corrosion inhibitors, *Prog. Org. Coat.* 62 (2008) 105–116, <https://doi.org/10.1016/j.porgcoat.2007.10.001>.
- [63] P. de Lima-Neto, A.P. de Araújo, W.S. Araújo, A.N. Correia, Study of the anticorrosive behaviour of epoxy binders containing non-toxic inorganic corrosion inhibitor pigments, *Prog. Org. Coat.* 62 (2008) 344–350, <https://doi.org/10.1016/j.porgcoat.2008.01.012>.
- [64] M.A. Langell, C.W. Hutchings, G.A. Carson, M.H. Nassir, High resolution electron energy loss spectroscopy of $MnO(100)$ and oxidized $MnO(100)$, *J. Vac. Sci. Technol. A: Vac., Surf., Films* 14 (1996) 1656–1661, <https://doi.org/10.1116/1.580314>.
- [65] M.C. Biesinger, B.P. Payne, A.P. Grosvenor, L.W.M. Lau, A.R. Gerson, R.S.C. Smart, Resolving surface chemical states in XPS analysis of first row transition metals, oxides and hydroxides: Cr, Mn, Fe, Co and Ni, *Appl. Surf. Sci.* 257 (2011) 2717–2730, <https://doi.org/10.1016/j.apsusc.2010.10.051>.
- [66] M.C. Manaka, M.S. Dhlamini, B.M. Mthudi, Dependence of manganese phosphorescence on crystal lattice sites of spinel aluminate hosts, *Phys. B Condens Matter* 550 (2018) 360–366, <https://doi.org/10.1016/j.physb.2018.08.034>.
- [67] D.F.; A.P.W. SHRIVER, *Química Inorgânica*, Bookman, Porto Alegre, 2003.
- [68] I.L. Weatherall, B.D. Coombs, 1992. *Skin Color Measurements in Terms of CIELAB Color Space Values*, 1992.
- [69] D.F.L. Horsth, J.O. Primo, M. Dalpasquale, C. Bittencourt, F.J. Anaissi, Colored aluminates pigments obtained from metallic aluminum waste, an opportunity in the circular economy, *Clean. Eng. Technol.* 5 (2021), <https://doi.org/10.1016/j.clet.2021.100313>.
- [70] J. de, O. Primo, K.W. Borth, D.C. Peron, V. de, C. Teixeira, D. Galante, C. Bittencourt, F.J. Anaissi, Synthesis of green cool pigments ($CoxZn_{1-x}O$) for application in NIR radiation reflectance, *J. Alloy. Compd.* 780 (2019) 17–24, <https://doi.org/10.1016/j.jallcom.2018.11.358>.
- [71] W. Bao, F. Ma, Y. Zhang, X. Hao, Z. Deng, X. Zou, W. Gao, Synthesis and characterization of Fe^{3+} doped $Co_0.5Mg_0.5Al_2O_4$ inorganic pigments with high near-infrared reflectance, *Powder Technol.* 292 (2016) 7–13, <https://doi.org/10.1016/j.powtec.2016.01.013>.
- [72] E. Song, X. Jiang, Y. Zhou, Z. Lin, S. Ye, Z. Xia, Q. Zhang, Heavy Mn^{2+} Doped $MgAl_2O_4$ phosphor for high-efficient near-infrared light-emitting diode and the night-vision application, *Adv. Opt. Mater.* 7 (2019), <https://doi.org/10.1002/adom.201901105>.
- [73] J. Yang, Y. Zhou, H. Ming, E. Song, Q. Zhang, Site-selective occupancy of Mn^{2+} enabling adjustable red/near-infrared multimode luminescence in olivine for dynamic anticounterfeiting and encryption, *ACS Appl. Electron Mater.* 4 (2022) 831–841, <https://doi.org/10.1021/acsaelm.1c01182>.